48th AIAA Aerospace Sciences Meeting Including the New Horizons Forum and Aerospace Exposition
4 - 7 January 2010, Orlando, Florida

AIAA 2010-1185

48th AIAA Aerospace Sciences Meeting, 4-7 January 2010, Orlando, Florida

Influence of Interactions Between Turbulence and Radiation on Transmissivities in Hypersonic Turbulent Boundary Layers

A. M. Feldick,[*] L. Duan,[†] M. F. Modest,[‡] M. P. Martín[§] and D. A. Levin[¶]

In the current paper, a high fidelity large eddy simulation solver is coupled to our modified line-by-line radiative transport equation solver to study the effects of absorption turbulence-radiation interations in a hypersonic turbulent boundary layer, representative of the Orion CEV entering Earth's atmosphere, at peak heating condition. The turbulent and radiation fields represent extreme conditions typical of Orion, as the simulated boundary layer represents the region of high turbulence coupled to region of highest incident radiation. A simplification in the calculation of molecular spectra with a single temperature property database in allows for tractable calculation of spectral properties. A comparison of wall directed intensities show the effects of absorption turbulence-radiation interactions due to radiation emitted in the shock layer is minimal, although a slight decrease in boundary layer transmissivities is predicted.

Nomenclature

C_f	Skin friction, dimensionless
E	Emission energy, W/m^3
F	Rotational term energy for a molecule, cm^{-1}
G	Vibrational term energy for a molecule, cm^{-1}
H	Shape factor, -
I	Radiative intensity, W/m^2-sr
J	Rotational quantum number, -
$L_{x,y,z}$	Domain length, m
M	Mach number, -
$N_{x,y,z}$	Number of columns, -
$N_{L,U}$	State population number density, m^{-3}
n_e	Electron number density, m^{-3}
n_k	Number density of atoms or molecules, m^{-3}
q	Turbulent kinetic energy, m^2/s^2
Q	Total partition function, -
Re_θ	Reynoldes number, $Re_\theta \equiv \frac{\rho_\delta u_\delta \theta}{\mu_\delta}$, dimensionless
$Re_{\delta 2}$	Reynoldes number, $Re_{\delta_2} \equiv \frac{\rho_\delta u_\delta \theta}{\mu_w}$, dimensionless
Re_τ	Reynoldes number, $Re_\tau \equiv \frac{\rho_w u_\tau \delta}{\mu_w}$, dimensionless
T	Temperature, K
u_τ	Friction velocity, m/s
V	Vibrational quantum number, -
z	Distance from body, m
δ	Boundary layer thickness, m
δ^*	Displacement thickness, m

---

[*] Graduate student, Department of Mechanical and Nuclear Engineering, The Pennsylvania State University

[†] Graduate student, Department of Mechanical and Aerospace Engineering, Princeton University, Visiting Student, Department of Aerospace Engineering, The University of Maryland

[‡] Shaffer and George Professor of Engineering, School of Engineering, The University of California, Merced, Associate Fellow AIAA

[§] Associate Professor, Department of Aerospace Engineering, The University of Maryland

[¶] Professor, Department of Aerospace Engineering, The Pennsylvania State University, Associate Fellow AIAA

ε_λ	Emission coefficient, W/m^3-Å-sr
ε^*_λ	Band emission cross-section, W/Å-sr
θ	Momentum thickness, m
κ_λ	Absorption coefficient, m^{-1}
$\kappa^*_{\lambda 1}$	Band absorption cross-section, m^2
$\kappa^*_{\lambda 2}$	Band absorption cross-section, m^2
λ	Wavelength, Å
ρ	Density, kg/m^3
σ	Standard deviation, -
τ	Transmissivity, -
ϕ	Line shape, Å^{-1}

I. Introduction

Accurate simulation of the hypersonic flow field surrounding, and heating loads onto, spacecraft during entry into planetary atmospheres or Earth return requires high-fidelity modeling of thermal radiation from the plasma in the shock layer, as well as radiation from within the boundary layer itself. It has long been recognized that at velocities exceeding 10 km/s radiation contributes significantly to the overall heat load, and that its accurate determination requires meticulous modeling of the plasma's and gas' spectral emission and absorption properties.[1] It is also well known today that, in the field of turbulent flames, there may be very strong interactions between radiation and the turbulent flow field, resulting in changes in radiative flux of 100% and more.[2] Whether and how such turbulence–radiation interactions (TRI) in a turbulent boundary layer on a hypersonic spacecraft affect the flow field and the heating loads on the craft is still unknown today. The effects of TRI are often considered with respect to two terms, emission TRI, and absorption TRI. Emission TRI is a local term, related to the turbulent variation of local properties such as temperature and number density. Absorption TRI, on the other hand, depends upon both the variation in local properties, as well as the variation in incident radiation due to the fluctuating turbulent flow field. The influence of TRI on transmitted radiation has been studied previously in the combustion community.[3,4] Prediction of TRI, and the associated radiative fluxes show strong sensitivity to the concentration and temperature, fields which vary greatly in the reacting regions of the flow. For emission TRI strong temperature variations result in significant changes in emission, due to the nonlinearity of emission with temperature ($E \sim T^4$). For absorption TRI turbulence chemistry interactions (TCI) also play a significant role owing to the less severe (more linear) dependencies of absorption coefficients on temperature and number densities.

In hypersonic flows radiation from the shock layer and from within the boundary layer will, due to radiation's "action at a distance," diminish local temperature fluctuations. But it is not known by how much, and how this feeds back to velocity fluctuations and overall turbulence levels. Existing RANS models require modification to account for the interrelationship between radiation, chemistry, and turbulence to a fidelity required for design analysis. In order to ensure accuracy, such modifications must be developed from first principles analysis, such as direct numerical simulation and large eddy simulation (DNS and LES, respectively) techniques coupled to high order nonequilibrium radiative transport solvers. Once the relevant terms have been identified via these analyses, their importance to design can be determined. If they are a significant source of uncertainty for Constellation mission objectives the results will be used to develop RANS-compatible subgrid models that can be incorporated into existing NASA design tools. The Constellation program which features manned missions to near Earth orbit, the Moon, and possibly Mars, are planned for the Orion crew exploration vehicle (CEV).

In the current work, LES is used to assess the effects of turbulence on the transmissivity of the boundary layer of radiation from the shock layer, using conditions typical of Orion crew exploration vehicle (CEV) during Earth entry. While significant absorption in the boundary layer is predicted, the effects of absorption TRI are predicted to be quite small.

II. Methodology

A. Model flow conditions

The Orion CEV is chosen as a representative flow for the study, and the finite volume code DPLR was used to model the full 3-D flow field as well as to establish boundary conditions for the flowfield and radiation analysis. The

M_δ	ρ_δ(kg/m^3)	T_δ(K)	T_w(K)	Re_θ	Re_τ	$Re_{\delta 2}$	θ(mm)	H	δ(mm)
0.153	0.011	9614	2607	68	388	189	3.4	0.1	0.257

Table 1. Dimensional bounday layer edge and wall parameters for large-eddy simulations

DPLR solution was generated by NASA Ames and was obtained using a two temperature model (T,T_V) by Park[5] and considers chemical reaction processes of 11 species: N, O, N^+, O^+, N_2, O_2, NO, N_2^+, O_2^+, NO^+ and e^-. The flow field is based on the CEV entering Earth's atmosphere at 9.5 km/s, at an altitude of 53 km, and angle of attack of 18 °. These conditions represent Earth entry, at peak heating. Turbulence is modeled using the two equation Menter SST model with compressibility correction. Figure 1 shows the entire computational domain for the DPLR finite-volume solution for Orion at peak heating, and Figs. 2(*a*,*b*) show the LES subdomain identified to explore turbulence-radiation interaction. The LES subdomain lies toward the front of the craft, where the temperature and electron number density are high and radiation is strong, as shown in Figs. 3, where the temperatures as well as number densities of radiating species (N, O, N_2, O_2, NO, N_2^+ for Earth reentry) along the line-of-sight indicated in Figs. 2(*b*) are plotted. For the presently estimated Orion peak heating conditions, it was found that the strong turbulence is limited to the aft region of the spacecraft, where radiation is weak. Therefore, to investigate a worst case scenario, a relatively large turbulence level($\sqrt{q}/u\tau \simeq 2.2$ or $\sqrt{q}/U\delta \simeq 7\%$), typical of that in the aft region, is prescribed to the selected LES sub-domain, where $q = u'^2 + v'^2 + w'^2$ is the turbulent kinetic energy. The analysis then represents a combination of strong turbulence together with strongest radiation to present a worst case scenerio for an Earth entry of Orion, or of a hypothetical case of a larger vehicle, to determine whether or not TRI may be of importance.

The boundary layer edge conditions and wall parameters for LES are given in Table 1, which provides boundary layer edge Mach number, density, and temperature (M_δ, ρ_δ, and T_δ, respectively). The table also gives the following boundary layer properties: momentum thickness, θ, shape factor, $H = \delta^*/\theta$ (δ^* is the displacement thickness), boundary layer thickness, δ (defined as the location where the flow velocity is 99% of that of the free stream), and Reynolds numbers are $Re_\theta \equiv \frac{\rho_\delta u_\delta \theta}{\mu_\delta}$, $Re_\tau \equiv \frac{\rho_w u_\tau \delta}{\mu_w}$, and $Re_{\delta_2} \equiv \frac{\rho_\delta u_\delta \theta}{\mu_w}$, where μ_δ is the boundary layer edge viscosity, μ_w is the viscosity at the wall, ρ_w density at the wall, and u_τ is the friction velocity.

B. Simulation details for LES

The governing unsteady fluid motion equations, namely chemical species mass, momentum and energy equations, are solved in conservative form. The LES form of the governing equations as well as subgrid-scale (SGS) terms are discussed in detail by Martin & Candler.[6] Since vibrational temperature is equal to translational temperature throughout the boundary layer (Fig. 3(*a*)), a one-temperature model is used for LES. Similar to DPLR, an 11-species reaction mechanism[5] is employed for gas-phase reactions and the Gupta-Yos mixing rule[7] is used for transport coefficients in LES. Complete thermal equilibrium of all species is assumed with equilibrium gas properties calculated using NASA LeRC curve fits;[8] an equilibrium catalytic boundary condition is used for species, i.e. species go to their equilibrium state at the given wall temperature.

The spatial derivatives are computed numerically using a fourth-order accurate, bandwidth-optimized WENO scheme.[9] To perform the numerical integration, a third-order accurate low-storage Runge-Kutta method by Williamson[10] is used. The viscous terms are computed using a fourth-order accurate central scheme. A description of the code and its validation is given in Martin[11] and Duan & Martin.[12]

The SGS terms are modeled using the one-coefficient dynamic mixed model of Martin, Piomelli and Candler,[13] which uses scale similarity terms coupled with a dynamic eddy viscosity and dynamic turbulent Prandtl number to model the SGS stresses and SGS heat flux. The SGS turbulent diffusion of kinetic energy is modeled as in Knight et al.[14] The SGS viscous diffusion of kinetic energy is expected to be of a smaller order of magnitude and is not modeled. The code has been validated in high speed boundary layer flow.[15]

The initial LES flow field is obtained by first initializing a DNS flow field and then filtering the DNS data and mapping it onto the LES grid. The DNS flow field is initialized following the initialization procedure by Martin,[11] with mean flow field parameters from the CEV solution, as described in Section A. The domain size ($L_x \times L_y \times L_z$), the grid size ($\Delta x \times \Delta y \times \Delta z$) and the number of grid points ($N_x \times N_y \times N_z$) for the initial DNS field are given in Table 2. The streamwise, spanwise, and wall-normal directions are taken to be x, y, and z, respectively. Uniform grid spacings are used in the streamwise and spanwise directions with constant Δx^+ and Δy^+, where the superscript ($^+$) indicates scaling

L_x/δ	L_y/δ	L_z/δ	Δx^+	Δy^+	z_2^+	α	N_x	N_y	N_z
9.3	1.9	15.2	7.8	2.9	0.31	1.061	440	240	120

Table 2. Grid resolution and domain size for the initial DNS field

with inner, or wall values. Geometric stretching is used in the wall-normal direction, with $z_k = z_2(\alpha^{k-1} - 1)/(\alpha - 1)$ with α chosen such that $z_{Nz} = z_{BL}$ (outer end of the LES sublayer).

After obtaining the initial DNS flow field, a top-hat filter is applied to each DNS variable along the three directions using

$$\overline{f}_i = \frac{1}{2n}\left(f_{i-\frac{n}{2}} + 2\sum_{i-\frac{n}{2}+1}^{i+\frac{n}{2}-1} f_i + f_{i+\frac{n}{2}} \right). \tag{1}$$

Therefore, $\overline{\Delta}_i = n\Delta_i$, where $\overline{\Delta}_i$ and Δ_i are the LES and DNS grid spacings, respectively, and n represents the nondimensional filter width. The trapezoidal rule is used in the wall-normal direction to account for the grid stretching. The filter width is $8\times4\times2$ in the streamwise, spanwise and wall-normal directions, respectively. With this filter width, the SGS carry about 20% of the turbulent kinetic energy.

Periodic boundary conditions in both streamwise and spanwise directions are used. Averages are computed over streamwise and spanwise directions of each field; then an ensemble average is calculated over 11 fields spanning around one nondimensional time unit. The time is nondimensionalized by δ/u_τ. Figure 4 shows the temperature profile and number density profiles of N and O in the flow field, along with RMS values for the fluctuating quantities for a single snap shot in time. As discussed in Duan et al.[16] the level of turbulence-chemistry interactions is very low in the present flowfield. As a result the RMS values for the fluctuating quantities are also fairly low ($<$ 15% of mean quantities), with the greatest variation being for N, while RMS values for temperature are about 10%.

C. Radiation Modeling

In order to study the effects of turbulence on the transmissivity of radiation from the shock layer, which enters the boundary layer domain from the outside, an irradiation boundary condition must be established. For this purpose the line-by-line (LBL) tangent slab solver of Feldick et al.[17] has been modified to first provide the spectral intensities hitting the edge of the boundary layer subdomain ($I_\lambda(z_{BL})$), and also calculate snapshots of the turbulent boundary layer transmissivity of the incoming radiation as it travels toward the CEV's surface.

The intensity of radiation emitted in the shock layer, traveling along a single direction toward the CEV's surface, attenuated by self-absorption along the way, may be written as[18]

$$I_\lambda(z) = \int_{-\infty}^{z} \varepsilon_\lambda(z')\exp\left(-\int_{z}^{z'} \kappa_\lambda dz''\right)dz' \tag{2}$$

where z is distance from the CEV surface along the surface normal, ε_λ is the emission coefficient and κ_λ the absorption coefficient in the shock layer, with contributions from all radiating species (N, O, N_2^+, NO, O_2 and N_2 for Earth reentry). Eq. (2) applies to the region from the edge of the boundary layer subdomain to outside of the shock layer, from $z(BL)$ in Fig. 5 to outside the computational domain To determine the transmissivity within the LES boundary layer, from $z(0)$ to $z(BL)$ in Fig. 5 local emission is not considered and, therefore, the local intensity inside the LES layer, due to radiation incident upon the outer edge of the boundary layer, attenuated by absorption, may be written as

$$I_\lambda(z) = I_\lambda(z_{BL})\exp\left(-\int_{z}^{z_{BL}} \kappa_\lambda dz'\right) \tag{3}$$

The solution of Eqs. (2), and (3) requires emission and absorption coefficients for all relevant spectral wavelengths. For emission and absorption coefficients of N, O, along with continuum contributions from N^+ and O^+, the databasing techniques of Sohn et al.[19] are used, including the effects of Stark broadening. Molecular species of N_2^+, NO, O_2 and N_2 are also considered, with the important bands included shown in Table 3. As described in Park[5] and Sohn et al.[19] molecular spectra depend upon 7 primary variables ($T_T, T_E, T_R, T_V, N_e, N_a/N_m, \lambda$), and each molecular band contains many lines ($O(10^3 - 10^6)$). The complexity of molecular spectra can add considerably to the computational

Table 3. Molecular Bands Included

Molec.	Name	Spectral Range (Å)
N_2^+	1^{-1} (1st negative)	2547 ~ 12000
N_2^+	Meinel	2749 ~ 12000
N_2	1^+ (1st positive)	2547 ~ 12000
N_2	2^+ (2nd positive)	2602 ~ 7229
N_2	Birge-Hopfield	870 ~ 1568
N_2	Birge-Hopfield 2	827 ~ 1889
N_2	Carrol-Yoshino	845 ~ 1240
O_2	Schummann Runge	1763 ~ 5919
NO	Beta	1681 ~ 9210
NO	Gamma	1653 ~ 5402

time. Figure 3 shows that for the entirety of the boundary layer, the vibrational temperature is essentially equal to the total temperature. If it is assumed that all temperatures are equal, the complexity can be reduced significantly. This assumption does not necessarily imply equilibrium radiation, with all states defined by Boltzmann distribution. The quasi-steady-state (QSS) approximation of Park[5] is still used, because the population of electrons, atoms, ions and molecules may or may not be in thermo-chemical equilibrium. In the current analysis, the LES boundary layer is composed of 110 cells in the x-direction, 120 cells in the y-direction, and 40 cells in the z-direction. Because the analysis is carried out at 11 separate flow times, $110 \times 120 \times 11 = 145200$ line-of-site calculations are required. Simplification of molecular spectral property retrieval is necessary to make accurate calculations tractable.

Simplifying the molecular band spectral calculations involves separating the temperature dependencies of each individual line strength and shape from the band electronic state populations. The emission coefficient for a particular band can be found from[19]

$$\varepsilon_\lambda = \sum_{i=1} \varepsilon_\lambda^c N_U \phi_{\lambda i} \tag{4}$$

where i is the line index, $\varepsilon_{\lambda i}^c$ is a constant for line i, and $\phi_{\lambda i}$ is the line shape for line i. If $\phi_{\lambda i}$ is taken to be the Doppler profile, which is accurate in the considered flow, as Stark broadening coefficients are low and pressure broadening is minimal, then $\phi_{\lambda i}$ is a function of wavelength and translational temperature only. N_U is the upper state population, which is different for each line in the band

$$N_U = \frac{N_U^e}{(Q_{VR})_U}(2J_U + 1)\exp\left[-\frac{hc}{k}\left(\frac{G(V_U)}{T_V} + \frac{F(J_U)}{T_R}\right)\right] \tag{5}$$

where N_U^e is the electronic upper state population, which can be determined via the quasi-steady state approximation, and is a constant for the entire band, $(Q_{VR})_U$ is the upper state total partition function, J_U is the rotational quantum number, V_U is the vibrational quantum number, F is the state rotational term energy, and G is state vibrational term energy. If $T_T = T_V = T_R = T_E = T$, then the upper state population can be written as

$$N_U = N_U^e B_1(T) \tag{6}$$

where

$$B_1(T) = \frac{1}{(Q_{VR})_U}(2J_U + 1)\exp\left[-\frac{hc}{k}\left(\frac{G(V_U)}{T} + \frac{F(J_U)}{T}\right)\right] \tag{7}$$

A temperature and wavelength dependent band emission cross-section can then be written as

$$\varepsilon_\lambda^*(T) = \sum_{i=1} \varepsilon_\lambda^c \phi_{\lambda i}(T) B_1(T), \tag{8}$$

and the emission coefficient for each band follows as

$$\varepsilon_\lambda = \varepsilon_\lambda^*(T) N_U^e \tag{9}$$

where $\varepsilon^*_\lambda(T)$ is a function of a single temperature and wavelength and N^e_U is precalculated, and constant over the entire band.

In the same way the absorption coefficient can be written as,

$$\alpha_\lambda = \sum_{i=1} \varepsilon^c_{\lambda i} N_U \frac{\lambda^5_{ci}}{2hc^2} \left(\frac{N_L}{N_U} - 1 \right) \phi_{\lambda_i}(T) \tag{10}$$

where

$$\frac{N_L}{N_U} = \frac{N^e_L (Q_{VR})_U}{N^e_U (Q_{VR})_L} \frac{2J_L + 1}{2J_U + 1} \exp\left[\frac{hc}{k} \left(\frac{G(V_U) - G(V_L)}{T_V} + \frac{F(J_U) - F(J_L)}{T_R} \right) \right] \tag{11}$$

Again, if one assumes the temperatures to be equal, then the lower-upper state population ratio can be expressed as

$$\frac{N_L}{N_U} = \frac{N^e_L}{N^e_U} B_2(T) \tag{12}$$

where

$$B_2(T) = \frac{(Q_{VR})_U}{(Q_{VR})_L} \frac{2J_L + 1}{2J_U + 1} \exp\left[\frac{hc}{k} \left(\frac{G(V_U) - G(V_L)}{T} + \frac{F(J_U) - F(J_L)}{T} \right) \right]. \tag{13}$$

The absorption coefficient can then be found from

$$\alpha_\lambda = \sum_{i=1} \varepsilon^c_{\lambda i} \frac{\lambda^5_{ci}}{2hc^2} N^e_U B_1(T) \left(\frac{N^e_L}{N^e_U} B_2(T) - 1 \right) \phi_{\lambda i}(T). \tag{14}$$

Defining band absorption cross-sections as

$$\alpha^*_{\lambda 1}(T) = \sum_{i=1} \varepsilon^c_{\lambda i} B_1(T) B_2(T) \frac{\lambda^5_c}{2hc^2} \phi_{\lambda_i}(T) \tag{15}$$

and

$$\alpha^*_{\lambda 2}(T) = \sum_{i=1} \varepsilon^c_{\lambda i} B_1(T) \frac{\lambda^5_c}{2hc^2} \phi_{\lambda i}(T) \tag{16}$$

the absorption coefficient for a band can be written

$$\alpha_\lambda = \alpha^*_{\lambda 1}(T) N^e_L - \alpha^*_{\lambda 2}(T) N^e_U \tag{17}$$

The band emission and absorption cross-sections $(\varepsilon^*_\lambda, \alpha^*_{\lambda 1}, \alpha^*_{\lambda 2})$ can be precalculated and stored in tables in terms of temperature and wavelength. Obtaining spectral coefficients at run time is then reduced to 3 table interpolations, and 3 multiplications, and one subtraction, as the electronic state populations N^e_U are calculated once and for all at the beginning of each line-of-sight calculation.

A strict LBL approach to resolving the spectral dependencies of RTE is computationally wasteful, as there are very few atomic lines, and the variation of continuum emission and absorption is minimal. Likewise, in the flow considered, the molecular absorption is optically thin, in all of the considered bands, with the exception of the bands of N_2, which emit very little, but absorb considerably in the Vacuum-Ultra-Violet regions. A variable step size is used in this application, with fine resolution of 120 points centered around each bound-bound line center, out to ± 30 Doppler half-widths of each atomic line, and a coarser resolution of 1.0Å for the continuum–molecular regime. The Doppler width is based on the maximum translational temperature along the line-of-sight. The values for $(\varepsilon^*_\lambda, \alpha^*_{\lambda 1}, \alpha^*_{\lambda 2})$ are stored at all spectral locations, with averaged values used for the continuum-molecular region, and spectrally resolved values in the atomic bound-bound regions. A sample calculation is presented in Fig. 6, which shows the wall-directed intensity and local emission along the line-of-site using temperatures and number densities taken directly from the DPLR solution. A LBL calculation is performed using the database of Sohn et al.[19] for both atomic and molecular spectra assuming the temperatures to be independent ($T_E = T_V$ and $T_T = T_R = T$). The LBL solution is performed using a fine resolution of 120 points centered around each bound-bound line center, out to ±30 Doppler half-widths of each atomic line, and a resolution of 0.05Å for the continuum–molecular regime. Figure 6 shows the local emission and wall–directed intensity for both the LBL and the averaged band-cross-section method. $I(z_{BL})$ is predicted to be 4.780 10^5 W/m^2 sr for the LBL solution, and 4.777 10^5 W/m^2 sr for the averaged band-cross-section method, while $I(0)$ is predicted to be 3.734 10^5 W/m^2 sr for the LBL solution, and 3.682 10^5 W/m^2 sr for the averaged band-cross-section method. The time required for the LBL calculation (130 cells) is 2000 seconds, while for the average band-cross-section method, the time required is 10 seconds.

Table 4. Wall intensities and Transmissivities I_{BL} = 4.7765 10^5 W/m^2 sr

Sample	$I(\langle T\rangle, \langle \underline{n}\rangle)$ W/m^2 sr	$\langle I(T, \underline{n})\rangle$	$\sigma(I(T, \underline{n}))$ W/m^2 sr	$\tau(\langle T\rangle, \langle \underline{n}\rangle)$	$\langle \tau(T, \underline{n})\rangle$	$\frac{\langle \tau(T, \underline{n})\rangle}{\tau(\langle T\rangle, \langle \underline{n}\rangle)}$
1	3.6917 10^5	3.6930 10^5	6.7838 10^2	7.729 10^{-1}	7.732 10^{-1}	1.004
2	3.6934 10^5	3.6774 10^5	5.7843 10^2	7.732 10^{-1}	7.699 10^{-1}	0.996
3	3.6950 10^5	3.6661 10^5	5.6520 10^2	7.736 10^{-1}	7.675 10^{-1}	0.996
4	3.6967 10^5	3.6661 10^5	5.6520 10^2	7.739 10^{-1}	7.675 10^{-1}	0.992
5	3.6982 10^5	3.6671 10^5	5.9089 10^2	7.743 10^{-1}	7.678 10^{-1}	0.992
6	3.6998 10^5	3.6772 10^5	5.0882 10^2	7.746 10^{-1}	7.699 10^{-1}	0.991
7	3.7014 10^5	3.6867 10^5	3.7187 10^2	7.749 10^{-1}	7.718 10^{-1}	0.994
8	3.7029 10^5	3.6918 10^5	3.6164 10^2	7.7523 10^{-1}	7.7291 10^{-1}	0.996
9	3.7044 10^5	3.6925 10^5	4.8393 10^2	7.7554 10^{-1}	7.7305 10^{-1}	0.997
10	3.7058 10^5	3.6895 10^5	6.2187 10^2	7.7585 10^{-1}	7.7244 10^{-1}	0.996
11	3.7073 10^5	3.6852 10^5	6.1622 10^2	7.7615 10^{-1}	7.7152 10^{-1}	0.994

III. Results

The intensity along the line-of-sight was then solved for each z-column in the LES domain, at each time step recorded in the flow. A wavelength dependent upper boundary condition is calculated and stored at the begining of each run, with a total incoming intensity at the upper boundary of 4.7765 10^5 W/m^2 sr. The average observed boundary intensity based on the fluctuating flow field was recorded ($\langle I(T, \underline{n})\rangle$), where $\underline{n}$ is a vector containing all species number densities, along with their standard deviation in observed wall intensity $\sigma(I(T, \underline{n}))$, for all 11 snap shots. Average flow quantities (temperatures and number densities) were computed, and the wall-directed $I_w = I(z = 0)$ intensity of the averaged flow values $I_w(\langle T\rangle, \langle \underline{n}\rangle)$ was determined, the results of which are listed in Table 4. The predicted values for the standard deviation are shown to be quite small, 2-3 orders of magnitude smaller than the average values, and often smaller than the difference between $\langle I(T, \underline{n})\rangle$ and $I(\langle T\rangle, \langle \underline{n}\rangle)$. This implies that there is very little variation in the intensity at the wall in the LES resolved solutions despite the much larger fluctuations in T and n (Fig. 4). While the difference between $\langle I(T, \underline{n})\rangle$ and $I(\langle T\rangle, \langle \underline{n}\rangle)$ is in most cases statistically significant, the differences are so small that they are not physically significant.

It has been observed in the field of combustion that turbulence-radiation interactions are negligible in the absence of chemical reactions.[20] Similarly here with relatively small fluctuations of T and $\underline{n}$ due to negligible turbulence chemistry interactions, turbulence radiation interactions are found to be negligible for transmitted intensities The transmissivity of the averaged flow values was calculated $\tau(\langle T\rangle, \langle \underline{n}\rangle)$, as was the average transmissivity based on the fluctuating values $\langle \tau(T, \underline{n})\rangle$. The transmissivity shows that there is significant absorption in the boundary layer. Again as seen from Table 4, there is very little difference in the transmissivity of averaged flow values and average transmissivity, with ratios of 1.000 ± .009. In general, a slight decrease in transmissivity as a result of TRI is observed. This is in contrast to the results obwerved in combustion applications by Krebs et al.[3,4] The effect, however, is quite small, again due to low variations in the turbulent flow field. A slight nonstationarity in the solution can also be observed, as $I(\langle T\rangle, \langle \underline{n}\rangle)$ and $\tau(\langle T\rangle, \langle \underline{n}\rangle)$ gradually increases. This effect is small, and due to the slowly evolving turbulent field.

IV. Concluding Remarks

In the current paper, a high fidelity LES solver is coupled to our modified line-by-line RTE solver to study the effects of absorption TRI in a hypersonic turbulent boundary layer, representative of the Orion CEV entering Earth's atmosphere. The turbulent and radiation boundary conditions used in this study represent extreme conditions, as the simulated boundary layer represents the region of highest turbulence coupled to region of highest incident radiation. A simplification in the calculation of molecular spectra with a single temperature property database in allows for tractable calculation of spectral properties. The effects of absorption TRI in the form of boundary layer absorption of radiation emitted in the shock layer are predicted to be small for the studied conditions with $\tau(\langle T\rangle, \langle \underline{n}\rangle)/\langle \tau(T, \underline{n})\rangle$ being very near to unity. The effects of absorption TRI due to non-local emission are therefore predicted to be negligible for any possible Earth entry conditions encountered by Orion.

References

[1] Whiting, E. E. and Park, C., “Radiative Heating at the Stagnation Point of the AFE Vehicle,” *NASA Technical Memorandom 102829*, 1990, pp. 395–418.

[2] Modest, M. F., “Multiscale Modeling of Turbulence, Radiation and Combustion Interactions in Turbulent Flames,” *International Journal of Multiscale Computational Engineering*, Vol. 3, No. 2, 2005, pp. 85–106.

[3] Krebs, W., Koch, R., Bauer, H. J., Kneer, R., and Wittig, S., “Effect of Turbulence on Radiative Heat Transfer Inside a Model Combustor,” *Proceedings of Eurotherm Seminar No. 37—Heat Transfer in Radiating and Combusting Systems 2*, 1994, pp. 349–362.

[4] Krebs, W., Koch, R., Ganz, B., Eigenmann, L., and Wittig, S., “Effect of Temperature and Concentration Fluctuations on Radiative Heat Transfer in Turbulent Flames,” *Twenty-Sixth Symposium (International) on Combustion*, The Combustion Institute, 1996, pp. 2763–2770.

[5] Park, C., “Non-equilibrium Hypersonic Aerodynamics,” *Wiley*, 1990.

[6] Martín, M. and Candler, G., “Subgrid-scale model for the temperature fluctuations in reacting hypersonic turbulent flows,” *Physics of Fluids*, Vol. 11, No. 9, 1999, pp. 2765–2771.

[7] Gupta, R., Yos, J., Thompson, R., and Lee, K., “A Review of Reaction Rates and Thermodynamic and Transport Properties for 11-Species Air Model for Chemical and Thermal Non-equilibrium Calculations to 30000K,” *NASA RP-1232*, 1990.

[8] Gordon, S. and McBride, B., “Computer Program for Calculation of Complex Chemical Equilibrium Compositions and Applications,” *NASA Reference Publication 1311*, 1994.

[9] Taylor, E., Wu, M., and Martín, M., “Optimization of Nonlinear Error Sources for Weighted Non-Oscillatory Methods in Direct Numerical Simulations of Compressible Turbulence,” *Journal of Computational Physics*, Vol. 223, 2006, pp. 384–397.

[10] Williamson, J., “Low-storage Runge-Kutta Schemes,” *Journal of Computational Physics*, Vol. 35(1), 1980, pp. 48–56.

[11] Martín, M., “DNS of Hypersonic Turbulent Boundary Layers. Part I: Initialization and Comparison with Experiments,” *Journal of Fluid Mechanics*, Vol. 570, 2007, pp. 347–364.

[12] Duan, L. and Martín, M., “An effective procedure for testing the validity of DNS of wall-bounded turbulence including finite-rate reactions,” *AIAA Journal*, Vol. 47, No. 1, 2009, pp. 244–251.

[13] Martín, M. P., Piomelli, U., and Candler, G. V., “Subgrid-Scale Models for Compressible Large-Eddy Simulations,” *Theoretical and Computational Fluid Dynamics*, Vol. 13, 2000, pp. 361–376.

[14] Knight, D., Zhou, G., Okong’o, N., and Shukla, V., “Compressible large eddy simulation using unstructured grids,” *AIAA Paper No.98-0535*, 1998.

[15] Martín, M. P., “Shock-Capturing and the LES of High-Speed Flows,” *CTR Annual Research Briefs*, 2000, pp. 193–8.

[16] Duan, L., Grube, N., Sohn, I., Martín, M. P., Modest, M. F., and Levin, D. A., “Effect of Turbulent Fluctuations on Radiative Heat Flux,” AIAA paper 2010-0354, 48th AIAA Aerospace Sciences Meeting, Jan. 2010.

[17] Feldick, A. M., Modest, M. F., and Levin, D. A., “Closely Coupled Flowfield–Radiation Interactions For Flowfields created during Hypersonic Reentry,” *AIAA Paper No. 2008-4104*, 2008, 40th AIAA Thermophysics Conference, Seattle, Washington.

[18] Modest, M. F., *Radiative Heat Transfer*, Academic Press, New York, 2nd ed., 2003.

[19] Sohn, I., Bansal, A., Levin, D. A., and Modest, M. F., “Advanced Radiation Calculations of Hypersonic Reentry Flows Using Efficient Databasing Schemes,” *Journal of Thermophysics and Heat Transfer*, 2009, submitted for publication.

[20] Mazumder, S. and Modest, M. F., “Turbulence–Radiation Interactions in Nonreactive Flow of Combustion Gases,” *ASME Journal of Heat Transfer*, Vol. 121, 1999, pp. 726–729.

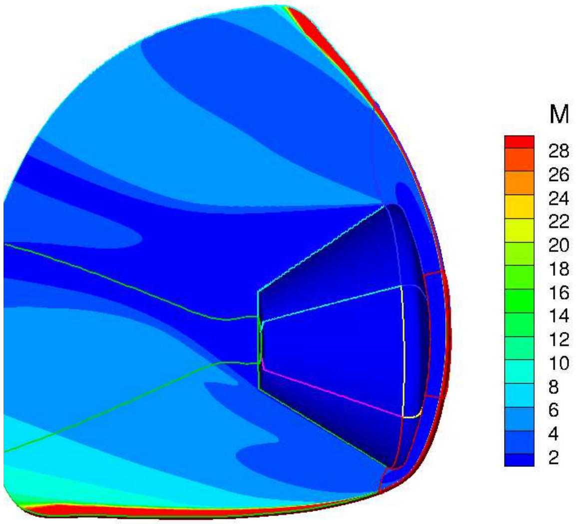

Figure 1. Contours of Mach number for a three-dimensional DPLR solution of Orion at peak-heating reentry conditions.

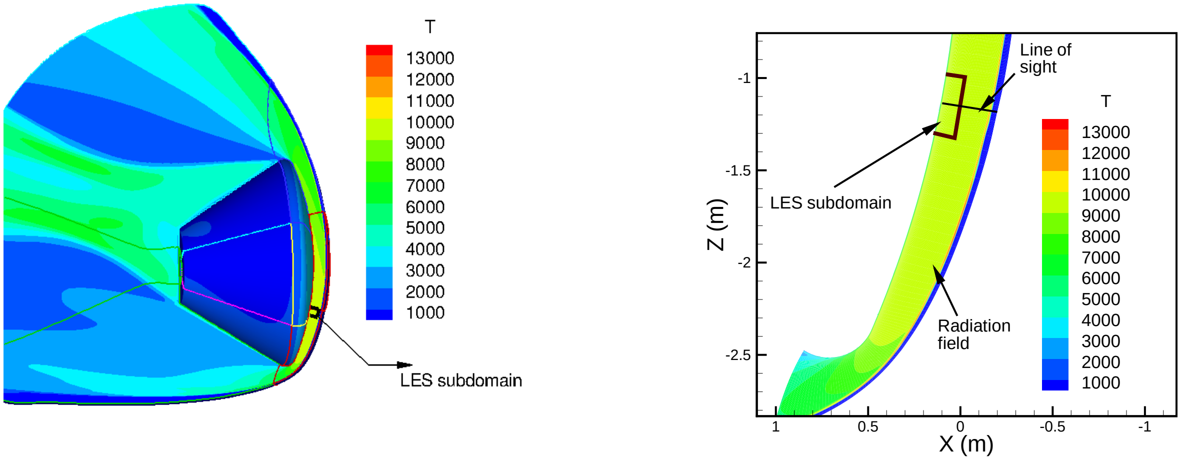

(a) (b)

Figure 2. LES subdomain from CEV solution.

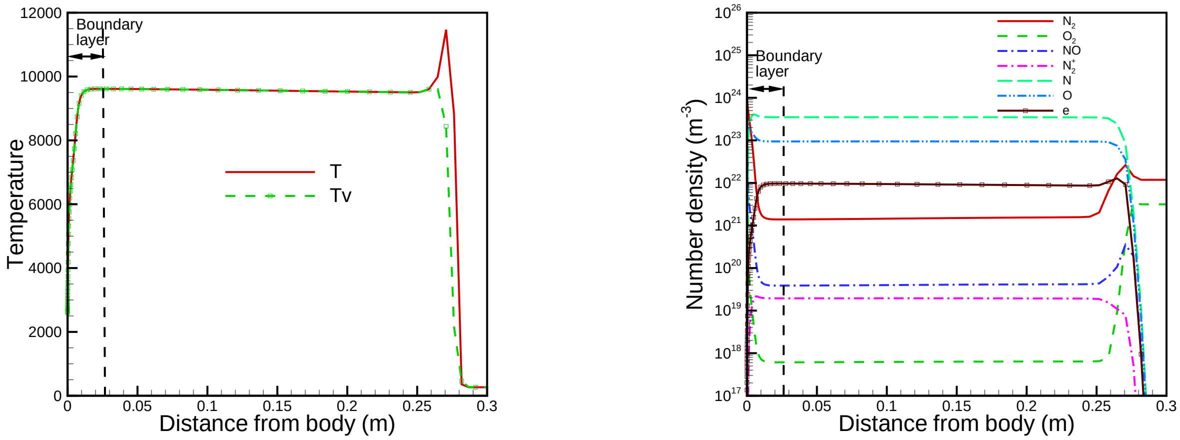

(a)

(b)

Figure 3. Temperatures and number densities along the line-of-sight indicated in Figure 2(*b*).

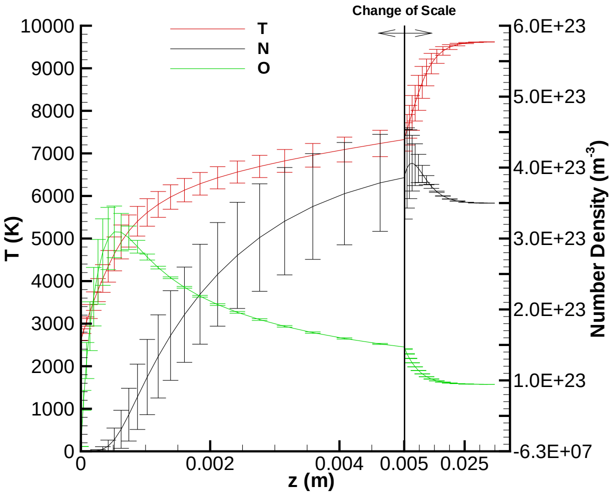

Figure 4. Boundary Profiles of Mean with RMS variations of Temperature and Number Density of N and O.

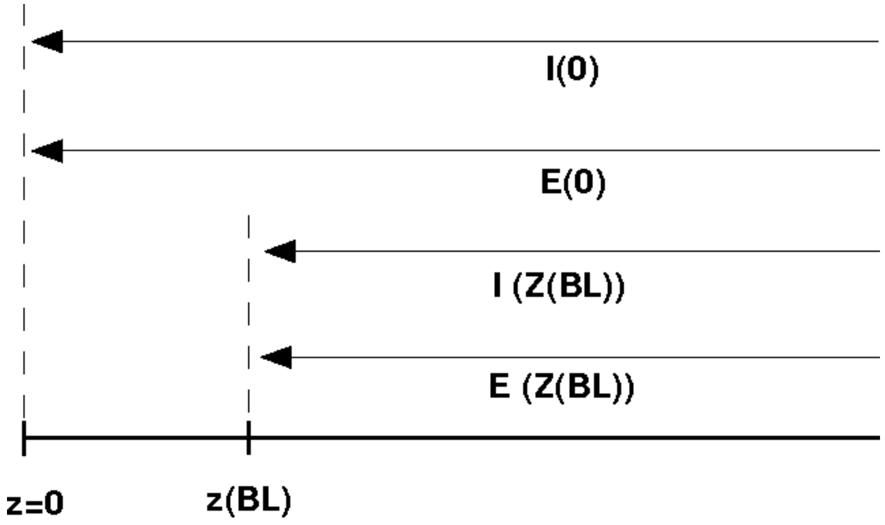

Figure 5. Schematic diagram of radiative intensity along a line-of-sight

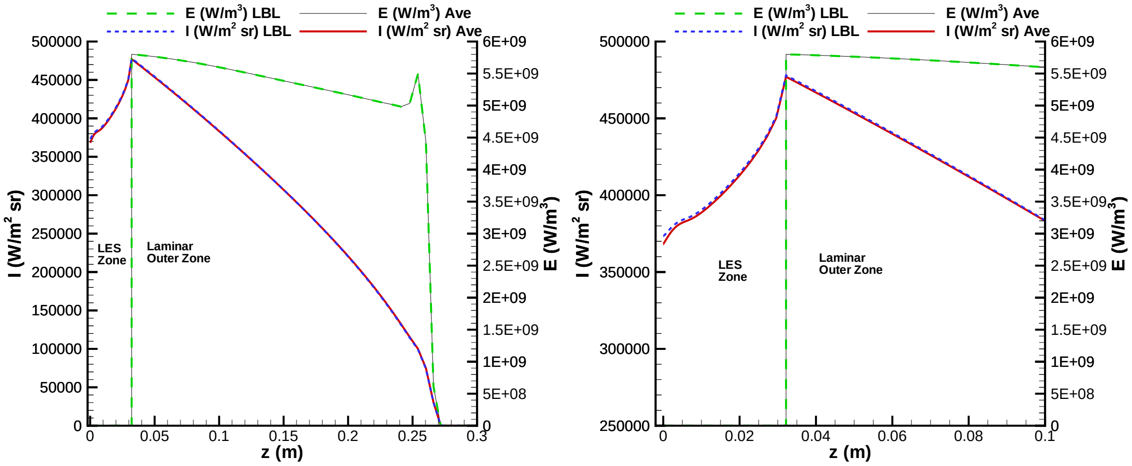

Figure 6. Radiative intensity along a line-of-sight located near the shoulder of the vehicle